Nanoscale

Accepted Manuscript

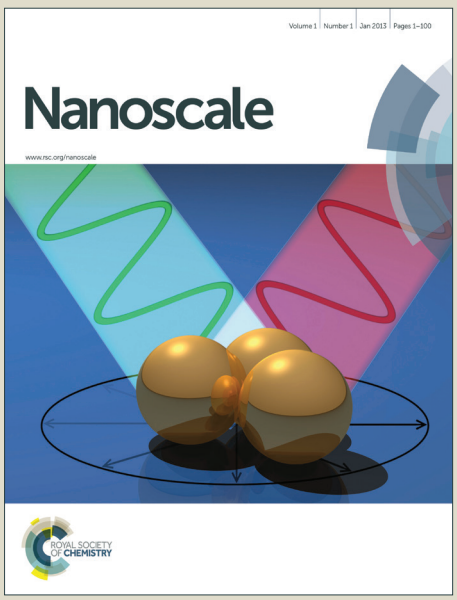

ROYAL SOCIETY OF CHEMISTRY

www.rsc.org/nanoscale

Cite this: DOI: 10.1039/c0xx00000x

www.rsc.org/xxxxxx

ARTICLE TYPE

Selectively enhanced red upconversion luminescence and phase/size manipulation *via* Fe^{3+} doping in $NaYF_4$:Yb,Er nanocrystals

Jing Tang,[a] Li Chen,[*a] Jing Li,[a] Zhe Wang,[a] Jiahua Zhang,[b] Ligong Zhang,[b] Yongshi Luo[b] and Xiaojun Wang[c]

Received (in XXX, XXX) Xth XXXXXXXXX 20XX, Accepted Xth XXXXXXXXX 20XX
DOI: 10.1039/b000000x

Red upconversion luminescence (UCL) is selectively enhanced by about 7 times *via* Fe^{3+} codoping into $NaYF_4$:Yb,Er nanocrystalline lattice. The maximum red-to-green ratio (R/G) as well as the overall integrated UCL intensity features at Fe^{3+} content of 20 mol%. The size and phase of nanocrystals are simultaneously manipulated *via* Fe^{3+} doping with various concentrations by a facile hydrothermal method. Contrary to the literature, the pure hexagonal phase appears when Fe^{3+} concentrations are from 5 to 20 mol%, meanwhile, the size of $NaYF_4$:Yb,Er nanocrystals reaches its maximum at 10 mol%. The intensified visible UCL especially the dominant red emission is mainly ascribed to the energy transfer (ET) from $|^2F_{7/2}$, $^4T_{1g}$ > (Yb^{3+}-Fe^{3+} dimer) to $^4F_{9/2}$ (Er^{3+}) states as well as the distortion of the crystalline field symmetry upon Fe^{3+} codoping. Dynamic investigation of $^4S_{3/2}$ and $^4F_{9/2}$ states under the pulsed laser excitation of 980 nm along with the diffuse reflectance data further convinces the proposed mechanism of UC processes. The results show the remarkable promise of Fe^{3+}-codoped $NaYF_4$:Yb,Er nanocrystals as an upconverting nanoprobe with high sensitivity and penetrability in deeper tissue for multimodal biomedical imaging.

1. Introduction

Lanthanide-doped upconversion nanocrystals (UCNCs) have recently attracted great attention not only for their fundamental scientific significance but also for their diverse potential applications, ranging from lasers,[1,2] color display[3, 4] to photovoltaics,[5, 6] especially in biomedical imaging.[7-9] *In vivo* imaging using upconverting emission is generally considered to be the next generation luminescence imaging technique due to its high resolution and sensitivity.[10] Manipulating the excitation and emission peaks in the range of so-called "optical windows" of the biological tissues,[11] red (600-700 nm) and near-infrared (700-1100 nm) regions, becomes extremely desirable, to avoid background autofluorescence. The emissions in this range can escape from the deeper tissue and subsequently be detected efficiently with higher signal-to-noise ratios.[12, 13] Among the host materials such as fluorides, oxides, vanadates and chlorides, hexagonal $NaYF_4$ is generally considered as the most efficient one due to its low phonon energy or low nonradiative loss and has been intensively investigated.[14] However, most of these systems such as Yb/Er doped $NaYF_4$, $NaLuF_4$ and $NaGdF_4$ often exhibit intense green emissions,[15, 16, 17] which is an apparent setback for *in vivo* bioimaging due to their less penetration depth.[16, 18] Therefore, it is of great importance to realize tunable red upconverted emission for bio-applications. Yb^{3+} ion as an efficient sensitizer with strong oscillator strength of the $^2F_{7/2}\rightarrow{}^2F_{5/2}$ transition coupled with transition metal ions has been co-doped into various hosts[19] to achieve intensified upconverted luminescence in green,[20] red[21] and white colors,[22] taking advantages of the specific energy levels of the rare earth ions, which are independent of crystal field, and the energy levels of the transition metal ions, which are tunable by manipulating the field strength. More recently, single band of dark red emission has been obtained through Mn^{2+} codoping into $NaLnF_4$:Yb,Er (Ln: Lu, Gd, Y) systems along with continuous rising of red-to-green intensity ratio as Mn^{2+} content increases.[11,13, 23, 24] Both intensified green and red emissions have also been observed in Fe^{3+}-codoped $NaGdF_4$:Yb,Er nanocrystals.[25] However, the insight of the precise effect of Fe^{3+} on the optical properties of the matrix materials remains not fully understandable or predictable.[26]

To meet the growing demand of biological applications, size/phase control of upconverting nanocrystals becomes necessary. Much effort has been devoted into this area and great achievements have been made.[27] Lanthanide and alkaline-earth are employed to tune crystal size and morphology even upconversion luminescence interpreted in terms of the dopant dipole polarizability and tailoring of the crystal fields.[28] Dopant ions with larger radius in comparison of substituted ions in the host lattice are generally considered to preferably induce hexagonal structure whereas the smaller dopant ions favour cubic phase.[23] However, to the best of our knowledge, Fe^{3+}-induced selective enhancement of upconversion luminescence with simultaneous size/phase manipulation has never been reported so far. In this contribution, selective enhancement of red upconversion luminescence and simultaneous size/phase

manipulation have been realized through Fe^{3+}-codoping in $NaYF_4$:Yb,Er nanocrystals. Energy transfer processes between Yb^{3+}-Fe^{3+} dimer and Er^{3+} as well as the distortion of crystalline field symmetry are proposed to better understand the enhancement. The quenching mechanism involved with Fe^{3+}-Fe^{3+} pairs has also been discussed at high Fe^{3+} doping levels. The results present a great promise of Yb-transition metal ion co-doped $NaYF_4$:Yb,Er upconverting nanostructures as a multimodal *in vivo* imaging agent in clinical applications.

2. Experimental

2.1 Materials

$Y(NO_3)_3$(99.99%), $Yb(NO_3)_3$ (99.99%), $Er(NO_3)_3$ (99.99%) and Oleic acid (OA, 90%) are purchased from Sigma-Aldrich. Anhydrous alcohol, $FeCl_3 \cdot 6H_2O$ and NaF are purchased from Sinopharm Chemical Reagent Co., Shanghai, China. All other chemical reagents are of analytical grade and are used directly with no further purification.

2.2 Synthesis of $NaYF_4$:Yb/Er/Fe UCNCs

$NaYF_4$: 18%Yb/2%Er/xFe (x=0, 5, 10, 20, 30, and 40 mol%) UCNCs are prepared by a hydrothermal method using oleic acid as a capping ligand and surface modifier.[23] At first, 0.3 g sodium hydroxide and 1.5 mL deionized water are mixed to form a clear and transparent solution, followed by adding 5 mL OA and 10 mL anhydrous alcohol. The mixed solution is continuous stirred for 20 min until transparent. The $RE(NO_3)_3$ and $FeCl_3$ in well-designed molar ratio are added into aforementioned solution with stirring at room temperature. In the case of $NaYF_4$:18 mol%Yb, 2 mol%Er, 5 mol%Fe nanocrystals, as an example, 0.75 mmol of $Y(NO_3)_3$, 0.18 mmol $Yb(NO_3)_3$, 0.02 mmol $Er(NO_3)_3$ and 0.05 mmol $FeCl_3 \cdot 6H_2O$ are introduced. After the solution becomes homogeneous, 4 mmol NaF is then slowly dropped into the flask accompanied by vigorous agitation for 20 min. Subsequently, the gelatinous solution is transferred into a 50 mL Teflon-lined stainless steel autoclave. The system is then sealed and continuously heated at 200 °C for 8 hours. After the reaction, the system is naturally cooled down to the room temperature, and thereafter the obtained products are washed three times with anhydrous alcohol and deionized water and dried in vacuum oven at 80°C for 12 hours. As for the sample without Fe^{3+} doping, the amount of $Y(NO_3)_3$ should be increased correspondingly.

2.3 Characterization

The crystallographic phase of the samples are characterized by powder XRD on a X-ray powder diffractometer (Rigaku D/Max IIA) with Cu Kα radiation (λ=1.54056 Å) at 6.0 degree/min. TEM images and selected area electron diffraction (SAED) patterns are obtained by a transmission electron microscope (JEM-2000EX) operating at an acceleration voltage of 200 kV. High-angle annular dark-field scanning TEM (HAADF-STEM) are carried out by using a FEI Tecnai F20 EM with an accelerating voltage of 200 kV equipped with an energy-dispersive spectrometer. Photoluminescence spectra are collected at room temperature with a spectrophotometer (Hitachi F-7000) equipped with a 980 nm CW diode laser. The decay curves are detected using a Triax 550 spectrometer (Jobin-Yvon) and recorded by a Tek-tronix digital oscilloscope (TDS 3052), while a 10 ns pulsed laser with tunable wavelengths from an optical parametric oscillator (OPO) pumped by a Nd:YAG laser (spectra-physics, GCR 130) is used as an excitation source. The UV-vis absorption spectra are obtained using a Cary 500 spectrometer. The photographs of the as-prepared UCNPs are recorded by a Canon digital camera under a CW diode laser excitation of 980 nm.

3. Results and discussions

Figure 1(a) shows the X-ray diffraction patterns of the as-prepared $NaYF_4$:18%Yb/2%Er nanocrystals tri-doped with 0-40 mol% of Fe^{3+} ions. There are no extra diffraction peaks can be observed when Fe^{3+} ions are added even at high doping levels exceed 30 mol% indicating that a homogeneous Fe-Y solid solution forms rather than additional possible undesired phase. Without Fe^{3+} ions incorporated, the X-ray diffraction pattern of $NaYF_4$:Yb/Er (18/2 mol%) sample can be indexed as a mixture phases of the cubic (JCPDS No. 06-0342) and hexagonal (JCPDS No. 16–0334) crystallographic structures of $NaYF_4$. In current fluoride host lattice, Fe^{3+} (r = 0.64 Å) are rationally considered to replace Y^{3+} (r = 1.159 Å) owing to the identical charge valence. On doping with increased Fe^{3+}concentrations, the transformation from cubic to hexagonal in the samples is evident. The pure hexagonal phase of $NaYF_4$ is obtained at the Fe^{3+} ion concentrations ranging from 5 mol% to 20 mol%. Whereas at higher doping levels i.e. 30 mol% and 40 mol% in this work, the cubic structure occurs featured by the crystallographic face peak (111) emergence even in the minority similarly in the case of Fe^{3+}-free sample (curve a in Figure 1(a)). There shows an apparent discrepancy between the herein results and the literatures,[23, 28] in which it is generally believed that introducing dopants with smaller radii compared to the substituted ions in the host lattice could induce hexagonal-to-cubic phase transformation. To understand this "anomalous" discrepancy we propose that it is not the size itself but the size difference between

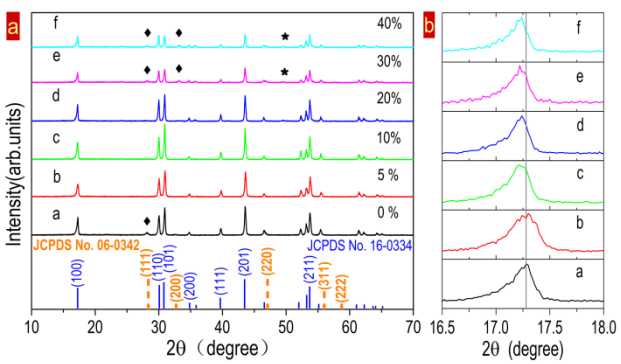

Fig.1 (a) XRD patterns of $NaYF_4$:Yb,Er nanocrystals codoped with Fe^{3+} at various contents of 0, 5, 10, 20, 30 and 40 mol% (curves a-f), some diffraction peaks of cubic phase are marked with ◆; asterisked peaks in curves e and f indicating the possible ErF_3 extra phase. (b) Magnified patterns in the diffraction angle range from 16.6 to 18 degree showing the shifting of hexagonal (100) crystal face.

the dopants and substituted ions in the host lattice that functions the phase manipulation mechanism. As an apparent evidence, hexagonal phase of $NaYF_4$ could not be obtained upon the substitution of larger radius size La^{3+} (r = 1.300 Å) for Y^{3+}.(ref: [28]) The radius disparity between La^{3+} and Y^{3+} is as significant as

0.141 Å, which is quite larger than that between Gd^{3+}(r = 1.193 Å), Sm^{3+}(r = 1.219 Å), Nd^{3+} (r = 1.249 Å) and Y^{3+} whose difference is of 0.034 Å, 0.06 Å, 0.09 Å, respectively. That mechanism works when the size difference is smaller than a certain value such as 0.141 Å but fails provided that it becomes even larger, for instance in current work, the difference between Y^{3+} and Fe^{3+} is 0.519 Å, which may dramatically impact on the dipole polarizability due to the electron cloud distortion thus breaks the phase evolution rule. This is also confirmed elsewhere by the consequences that hexagonal phase of $NaYF_4$ nanocrystal still remains even if smaller size Mn^{2+} (r = 0.810 Å) is introduced into the host lattice to replace larger size Y^{3+} ion (the radius difference of Y^{3+} and Mn^{2+} is 0.349 Å) until the Mn^{2+} content increases up to 44 mol%.[24]

Moreover, the diffraction peaks of hexagonal (100) crystal face shifts slightly to the higher-angle side as shown in Figure 1(b), a magnified region of diffraction peaks, due to the decreased unit-cell volume as well as the interplanar distance indicating that Fe^{3+} ions adopt substitutional sites for larger radius Y^{3+} at lower content of 5 mol%. Whereas with more and more Fe^{3+} are introduced, Fe^{3+} occupying the interstitial sites could lead to the host lattice expansion, the unit-cell volume and the interplanar distance increase, therefore the (100) peak shifts gradually toward the lower-angle side, which is shown in Figure 1(b) (curves c-f). Such shrinking and expanding effects on the unit-cell volume caused by introduced dopants into host lattice occupying substitutional and interstitial sites correspondingly are also reported in the case of Li^+ doped $NaGdF_4$ and $NaYF_4$ nanocrystals.[29] It is worth noting that both these two occupancies of Fe^{3+} ions located in the host matrix can tailor the local crystal field around Er^{3+} which gives rise to the breaking of the forbidden transition in favour of the irradiative *f-f* intra-configuration transitions of the rare earth ions.

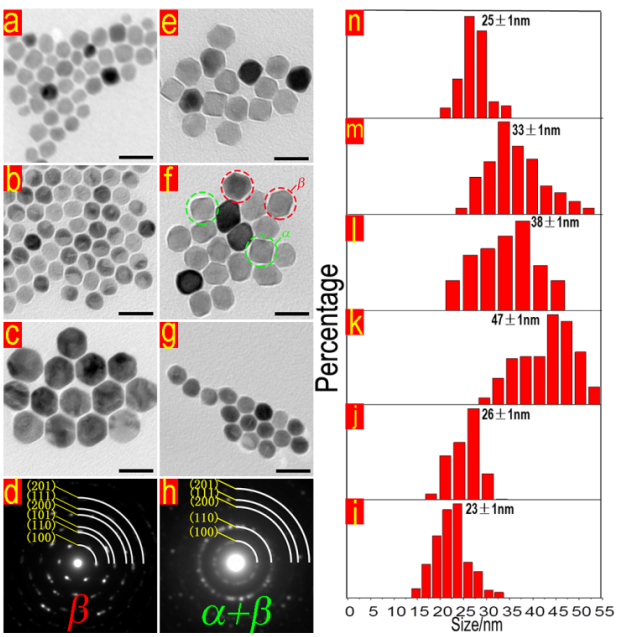

Fig. 2 (a-c, e-g) Typical TEM images of $NaYF_4$:Yb,Er nanocrystals doped with Fe^{3+} different contents (0, 5, 10, 20, 30 and 40 mol%) and (i-n) the corresponding size distribution patterns of tridoped $NaYF_4$ UCNCs, respectively; (d, h) the representative SAED taken from (c) and (f) indicating the pure hexagonal phase and the mixed hexagonal and cubic nanostructure, respectively. Scale bars are 50 nm for all images.

Transmission electron microscopy (TEM), SAED and size distribution analysis are performed as shown in Figure 2 to further clarify the size/phase evolution of the $NaYF_4$:Yb,Er nanocrystals co-doped with various Fe^{3+} contents. All the typical TEM images of as–synthesized nanocrystals exhibit excellent monodispersity with the average diameters in the range of 23 nm to 47 nm when adding Fe^{3+} from 0 to 40 mol%. The maximum size of 47 nm occurs as Fe^{3+} doping concentration reaches 10 mol% and subsequently the size growth in reverse for Fe^{3+} contents of 20-40 mol% as demonstrated in Figure 2 (l)-(n). Simultaneously, the mixture of hexagonal and cubic crystalline phases at 0 mol% is tuned to pure hexagonal nanostructure at Fe^{3+} contents of 5-20 mol% and with Fe^{3+} doping level being increased up to 30 mol% and 40 mol% the mixed structures can be observed again. This phase transformation trend is confirmed in well-indexed SAED patterns of mixture phases shown in Figure 2(h) and pure hexagonal phase in Figure 2(d) respectively, which is consistent with the aforementioned XRD data. These results indicate that the phase and size of $NaYF_4$:Yb,Er can be conveniently manipulated *via* adjusting the doped Fe^{3+} contents. The crystalline size increases firstly as in Fe^{3+}-free to 10 mol% Fe^{3+} samples and decreases subsequently when Fe^{3+} is further introduced up to 40 mol%, which is quite different from the literature,[23] in which smaller size Mn^{2+} ions doped into $NaLuF_4$ nanocrystals can induce a continuous growth of the particles. It is natural and rational to understand the size increase upon Fe^{3+} codoping by the formation of transient electric dipoles originated from smaller substitution ions for larger ions in the host lattice, which can accelerate the diffusion of F^- from the solution to the grain therefore enlarge the nanoparticles. Whereas the discrepancy of size evolution between the literature and current work could be mainly ascribed to the saturation of such transient electric dipoles by increased Fe^{3+} occupancies located at interstitial sites, then inducing a reverse direction with negative poles outward resulting in a reduction of the $NaYF_4$ nanocrystal size by repulsing the F^- ions from the solution to the grain.[13, 24]

It is highly desirable to tune the upconverting sharp emission bands into red or near-infrared region since intense red UCL is beneficial for *in vivo* bioimaging with respect to high bio-tissue penetrability and low tissue absorption.[30] P. Ramasamy and coworkers recently reported the intense visible UCL in tri-doped $NaGdF_4$:Yb,Er,Fe nanocrystals as well as the application in bioimaging. However, it still remains a great challenge to achieve selective enhancement of red UCL in Yb/Er doped system with controlled synthesis of simultaneous size/phase manipulation. Figure 3 shows the effect of various Fe^{3+} codoping contents on the UCL of $NaYF_4$:Yb,Er nanocrystals. Upconversion emission spectra of samples with and without Fe^{3+} codoping shown in Figure 3(a) exhibit three distinct visible bands at 510-534 nm, 534-558 nm and 630-690 nm stemming from $^2H_{11/2}\rightarrow{}^4I_{15/2}$, $^4S_{3/2}\rightarrow{}^4I_{15/2}$, and $^4F_{9/2}\rightarrow{}^4I_{15/2}$ transitions of Er^{3+} ions, respectively. The digital photographs of Fe^{3+}-free and 20 mol% Fe^{3+} doping samples under a CW diode laser excitation of 980 nm are presented in the Inset of Figure 3(a), clearly demonstrating the corresponding yellow and dramatically enhanced red emissions respectively, which can be seen by naked eyes in consistent with the UCL spectra. This selective enhancement effect upon various Fe^{3+} doping concentration in the range from 0, 5, 10, 20, 30 to 40

mol% is apparently depicted in Figure 3(b), in which the integrated intensities of the green, red even overall UCL are plotted as a function of Fe^{3+} concentration. Both the red and overall upconversion emissions are significantly enhanced to the maximum at Fe^{3+} content of 20 mol% by ~7 and ~4.5 times, respectively, whereas the green emission intensity merely shows a small scale increase and rises up to its maximum at 20 mol% Fe^{3+} doping level as well.

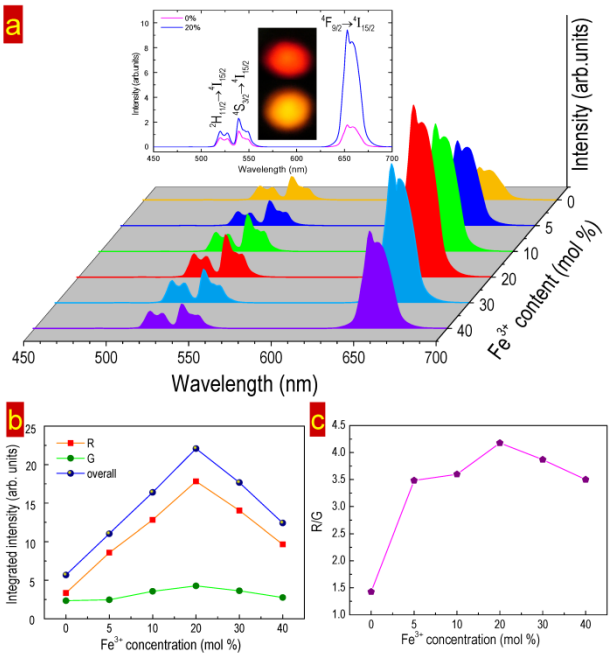

Fig. 3 (a) UCL spectra of $NaYF_4$:18%Yb, 2%Er, xFe^{3+} (x=0, 5, 10, 20, 30 and 40 mol%) nanocrystals under the excitation of 980 nm diode laser. (b) The integrated intensity of red, green and overall UC emissions as a function of Fe^{3+} doping concentration. (c) Calculated R/G ratio dependent on the Fe^{3+} contents. The inset of (a) presents the UCL spectra of Fe^{3+}-free and 20 mol% Fe^{3+} codoped $NaYF_4$:Yb,Er nanocrystals as well as the corresponding digital photographs (upper: 20 mol% Fe^{3+}; lower: Fe^{3+}-free sample).

The optimized R/G of integrated UCL intensity can be achieved in the sample containing 20 mol% Fe^{3+} ions as illustrated in Figure 3(c) and subsequently the R/G decreases as the Fe^{3+} contents increase from 30 to 40 mol%. The decrease of UCL intensity and R/G at higher Fe^{3+} contents (i.e.>20%) could be resulted from the exchange interaction between Fe^{3+} ions which is depicted in the left part of Figure 3c and significant distortion of the lattice which induces the concentration quenching thus reducing the UCL intensity.[25]

To reveal the upconverting photon excitation mechanism, the integrated intensities of red, green as well as the overall UCL in $NaYF_4$:Yb,Er nanocrystal samples without Fe^{3+} ions and with 20 mol% doping are recorded and shown respectively in Figure 4 (a),(b) as a function of the 980 nm excitation power in log-log plots. It is well known in the UC process that the UC emission intensity in dependence on the excitation power can be described by the following equation:[19, 31] $I_{UCL} \propto P_{NIR}{}^{n}$, where n is the number of pump photons absorbed per upconversion photon emitted, I_{UCL} is the UCL intensity, P_{NIR} is the pump power of near infrared laser.

In Fe^{3+}-free sample of $NaYF_4$:Yb,Er nanocrystal (Figure 4(a)) the slope values of $^4F_{9/2}\rightarrow{}^4I_{5/2}$, $^4S_{3/2}\rightarrow{}^4I_{15/2}$, and $^2H_{11/2}\rightarrow{}^4I_{15/2}$ upconverting emission bands are 1.67, 1.34 and 1.83, respectively. For 20 mol% Fe^{3+} doped $NaYF_4$:Yb,Er nanocrystals (Figure 4(b)) the corresponding slopes are 1.38, 1.05 and 1.68 which are slightly lower than those in Fe^{3+}-free sample. The results indicate that green and red upconversion luminescence of Er^{3+} are ascribed to two photons processes. In $Yb^{3+}/Er^{3+}/Fe^{3+}$-tridoped $NaYF_4$ nanocrystals, the n values for the green UCL much lower than 2, which suggests there may probably be Yb^{3+}-Fe^{3+} dimer formed in this sample designated as $|^2F_{7/2}, {}^6A_{1g}>$, $|^2F_{5/2}, {}^6A_{1g}>$ and $|^2F_{7/2}, {}^4T_{1g}>$, $|^2F_{7/2}, {}^4T_{2g}>$. The first step feeding from the $|^2F_{7/2}, {}^4T_{1g}>$ level of Yb^{3+}-Fe^{3+} dimer to the ($^4F_{7/2}$, $^4S_{3/2}$) levels of Er^{3+} ions can remarkably increase the population of the ($^4F_{7/2}$, $^4S_{3/2}$) levels, so as to result in the n values for the green UCL In $Yb^{3+}/Er^{3+}/Fe^{3+}$-tridoped sample lower than that in Fe^{3+}-free sample.[32]

Yb^{3+} ions are preferably incorporated into the host to sensitize the activators that generate visible upconversion emissions upon near infrared laser excitation, and can dramatically overcome the inefficient absorbability owing to the Laporte-forbidden $4f-4f$ transitions of lanthanides, most frequently for instance, known as Er^{3+} ions in fluoride matrix. The upconversion process mechanism in $NaYF_4$:Yb,Er nanocrystals doped with and without Fe^{3+} is illustrated in Figure 4(c) at the lower part of which a colored arrow indicates the Fe^{3+} content variation. In Fe^{3+}-free system, the electrons in $^2H_{7/2}$ level of Yb^{3+} are excited to the $^2H_{5/2}$ excited states by absorbing the 980 nm laser excitation energy, followed by the energy transfer from the excited Yb^{3+} ions to Er^{3+} in $^4I_{15/2}$ ground state making the $^4I_{11/2}$ populated. Subsequently, the excited electrons in $^4I_{11/2}$ level of Er^{3+} undergo two processes as following: one is the excited state absorption to the $^4F_{7/2}$ level

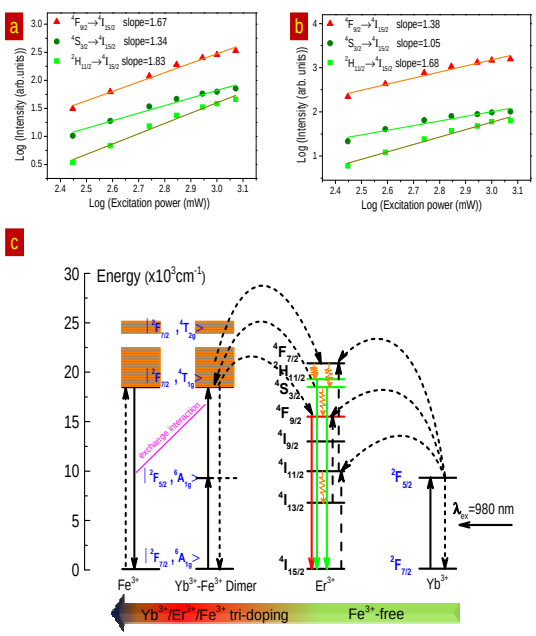

Fig. 4 Pump power dependence of the red ($^4F_{9/2}\rightarrow{}^4I_{5/2}$), green ($^4S_{3/2}\rightarrow{}^4I_{15/2}$ and $^2H_{11/2}\rightarrow{}^4I_{15/2}$) UCL of Fe^{3+}-free (a) and 20 mol% Fe^{3+} codoped (b) $NaYF_4$:18%Yb,2%Er nanocrystals. (c) Schematic energy level diagram showing the proposed upconversion mechanism of Fe^{3+}-free and codoped $NaYF_4$:Yb,Er nanocrystals. The color arrow in the lower part schematically indicating the Fe^{3+} contents variation trend from 0 to 5-40 mol%.

and the other nonradiative relaxation to the $^4I_{13/2}$ level. In the former case, the excited electrons populated at $^4F_{7/2}$ state relax rapidly to the $^2H_{11/2}$ and the $^4S_{3/2}$ states through multiphonon relaxation steps, leading to the green emission bands (510-534 nm, 534-558 nm). In the latter case, the electrons at $^4I_{13/2}$ state jump to $^4F_{9/2}$ state by absorbing additional excitation energy migrated from Yb^{3+} following a radiative transition process to the ground state $^4I_{15/2}$ of Er^{3+} producing the red emission (630-690 nm).

Fe^{3+} belongs to transition metal ion with outer $3d^5$ electron configuration. When Fe^{3+} ions are introduced into fluoride host with octahedral coordination, the energy levels of ferric ions dependent on crystal field strength can be illustrated by Tanabe-Sugano energy diagram.[33] With regard to the $Yb^{3+}/Er^{3+}/Fe^{3+}$-tri-doped system hosted by $NaYF_4$ nanocrystals, the supposed energy levels diagram is depicted on the left side of Figure 4(c) in which some new energy levels are formed owing to the mixed electron wavefunctions of Yb^{3+} and Fe^{3+}. Although the sensitizing process merely through Yb^{3+} ions as in Fe^{3+}-free system could not be thoroughly excluded, the prominent selective enhancement of red UC emission is obtained mainly by the codoped Fe^{3+} ions. It may originate from the sensitization *via* Yb^{3+}-Fe^{3+} dimer complex, which is quite similar to the recent reports on enhancement of green,[20] red[21] emissions as well as the white light achievement[22] involved Yb^{3+}-transition metal ions dimer system. The selectively enhanced red emission and increased R/G ratio with increasing doping content of Fe^{3+} are ascribed to the back energy transfer from Yb^{3+}-Fe^{3+} dimer to Er^{3+}, which has been reported on the observation of enhanced red emission in Mn^{2+}-codoped $NaLuF_4$:Yb,Er and $NaYF_4$:Yb,Er systems.[11, 13] This explanation in Fe^{3+}-codoped system, nevertheless, requires evidence given by further study in the future.

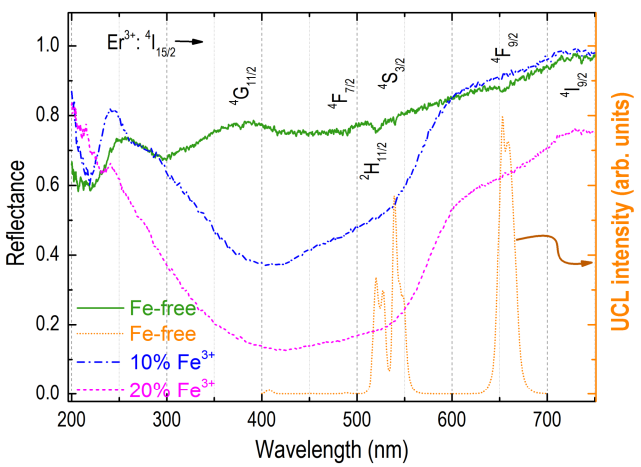

Fig. 5 Diffuse reflectance spectra for Fe^{3+}-free and xFe^{3+} codoped $NaYF_4$:Yb,Er (x= 10 mol% and 20 mol%) nanocrystals as well as UCL spectrum for Fe^{3+}-free sample (orange line).

Figure 5 shows the diffuse reflectance (DR) spectra for Fe^{3+}-free and xFe^{3+} co-doped $NaYF_4$:18%Yb, 2%Er (x= 10 mol% and 20 mol%) samples. The bold green line in Figure 5 represents the DR spectrum for Fe^{3+}-free sample. The slender absorptions in the range of 200 to 750 nm are attributed to the transitions of Er^{3+} from the $^4I_{15/2}$ ground state to the upper excited state levels ($^4G_{11/2}$, $^2H_{11/2}$, $^4S_{3/2}$, $^4F_{9/2}$, $^4I_{9/2}$), respectively. With the co-doped Fe^{3+} concentration increasing, the broad absorption band from 250 nm to 600 nm, which can be ascribed to the absorption of Yb^{3+}-Fe^{3+} dimer complex, appears and enhance gradually, indicating the increased Fe^{3+} ions incorporated into lattices. On the basis of diffuse reflectance data, the energy level diagrams of Yb^{3+}-Fe^{3+} dimer can be depicted approximately as shown in Figure 4. Furthermore, the DR spectra exhibit that the strong absorption of Yb^{3+}-Fe^{3+} dimer complex exists the larger spectral overlap with the green emission in UCL spectrum for Fe^{3+}-free sample. It implies the green emission can be re-absorbed by the Yb^{3+}-Fe^{3+} dimer complex.

The spectra exhibit, with the remarkable enhancement of red emission, an intensity rise of green emission in a finite scope as well with Fe^{3+} doping concentration increasing up to 20 mol% (Figure 3(b)). It is generally believed that the crystalline field symmetry in the vicinity of lanthanides activators dramatically impacts on the upconversion luminescent intensity by affecting the electronic transition probabilities. In current work, the surrounding environment has been tailored by Fe^{3+} codoping which is apparently evident in aforementioned XRD analysis. Figure 1 shows that the shifting of diffraction angle indicates the substitutional and interstitial sites of Fe^{3+} in the crystal lattice, as a consequence leading to the asymmetric environment around rare earth ions which favors the radiative transitions. XPS studies of Fe^{3+}-codoped $NaGdF_4$:Yb,Er nanoparticles turn out to support the bond length changing arise from the Fe^{3+} introducing.[25] E. He and coworkers calculated the Ω_2 parameter according to Judd-Ofelt theory in Mn^{2+}-free and Mn^{2+}-doped $NaYF_4$:Yb,Er nanocrystals and found that this parameter increased remarkably after high level doping of Mn^{2+}, implying the great reduction of local symmetry.[24] Therefore, we can rationally deduce that in our tridoping system the tailored crystal field symmetry *via* Fe^{3+} doping to asymmetry of local surroundings is responsible for the enhancement of overall UCL intensity as ferric ions increase up to 20 mol% (Figure 3(b)). When the Fe^{3+} concentration further increases from 30 mol% to 40 mol% green, red and overall UCL intensities even R/G ratio drop down as shown in Figure 3 (b), (c). That is because the heavy doping of Fe^{3+} could evoke the possible exchange interaction between Fe^{3+} ions and the significant distortion of the lattice as a result expanding the distance between Yb^{3+} and Er^{3+} which leads to the UCL quenching.

To further clarify the mechanism of selective enhancement of red UC emission in Fe^{3+}-codoped $NaYF_4$:Yb,Er nanocrystals, the decay curves of Er^{3+}: $^4S_{3/2}$ and $^4F_{9/2}$ states for Fe^{3+}-free and 20 mol% Fe^{3+} doped $NaYF_4$:Yb,Er samples under pulsed laser excitation of 980 nm are performed at room temperature. Figure 6(a) and Figure 6(b) show the decay curves by monitoring Er^{3+}: $^4F_{9/2}\rightarrow{}^4I_{15/2}$ and $^4S_{3/2}\rightarrow{}^4I_{15/2}$ transitions, respectively. Each transient exhibits a typical rise and decay. This is a clear indication of the energy-transfer process. Simplified model that predicts the time dependence of UCL emission intensity $I(t)$ after short pulse excitation can be proposed:

$$I(t) = A\left(e^{-t/\tau_d} - e^{-t/\tau_r}\right)$$

Where A is an emission intensity factor, τ_r and τ_d represent the rise and decay times of transient, respectively. The transient decay section is non-single exponential, the effective fluorescent decay time τ_d is determined using the following equation where

I(t) represents the luminescence intensity at t time.

$$\tau = \frac{\int_0^\infty I(t)tdt}{\int_0^\infty I(t)\,dt}$$

The decay times for the green and red emissions are calculated by integrating the area under the corresponding decay curves with the normalized initial intensity, reaching the corresponding lifetime exhibited in Figure 7. The best fit for the red and green emission get the rise times (τ_r) shown in the Insets of Figure 6. Figure 6(a) shows the rise times of red emission: τ_{r0} ~ 23 μs and τ_{r20} ~ 37 μs. Figure 6(b) shows the rise times of green emission: τ_{r0} ~ 3.6 μs and τ_{r20} ~ 15 μs. The short τ_r is decided by the self-decay of level. The long τ_d depends mainly on the UCL decay function which is mainly determined by the product of the decay functions of the Yb^{3+}: $^2F_{5/2}$ and Er^{3+} intermediate states.[34] The green and red emission lifetimes in 20 mol% Fe^{3+}-codoped $NaYF_4$:Yb, Er samples are longer than those of the Fe^{3+}-free sample, which confirms the presence of new-path energy transfer from Yb^{3+}-Fe^{3+} dimer complex to Er^{3+} in present system. The level lifetime is proportional to population.[35] The longer values τ_d indicates the stronger red and green UCL in Fe^{3+}-codoped $NaYF_4$:Yb,Er nanocrystals. Due to re-absorpion by the Yb^{3+}-Fe^{3+} dimer complex, the green emission intensity does not increase remarkably. This result agrees with the emission intensity variation shown in Figure 3(a).

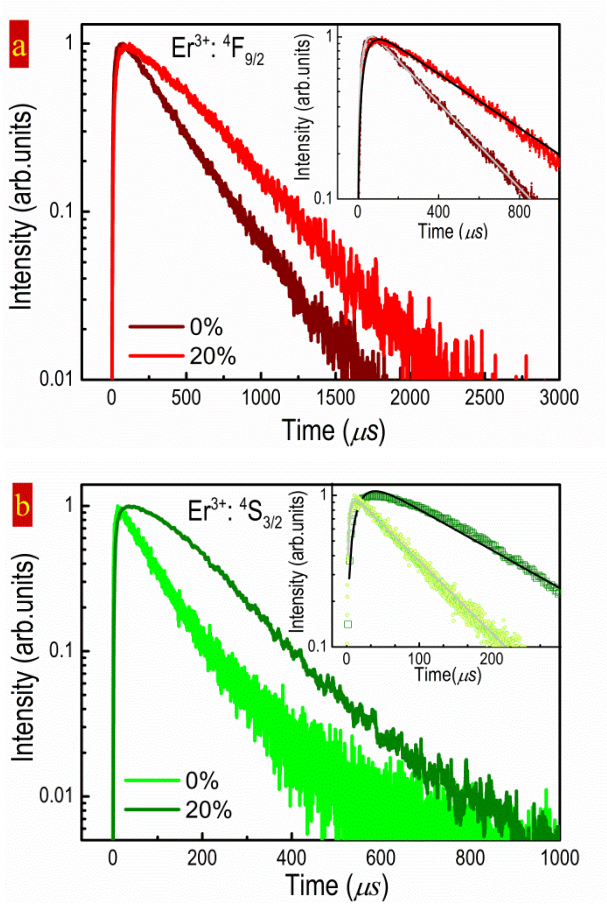

Fig. 6 Time evolutions of Fe^{3+}-free and 20 mol% Fe^{3+} doped $NaYF_4$:Yb,Er samples by monitoring the $^4F_{9/2} \rightarrow {}^4I_{15/2}$ (a) and $^4S_{3/2} \rightarrow {}^4I_{5/2}$ (b) transitions, respectively, under the excitation of a 10 ns pulsed laser at 980 nm from OPO.

In addition, the Fe^{3+} concentration dependence of corresponding UCL lifetimes of Er^{3+}: $^4S_{3/2}$ and $^4F_{9/2}$ states in $NaYF_4$: 18%Yb, 2%Er, xFe nanocrystals (x = 0, 5, 10, 20, 30 and 40 mol%) are shown in Figure 7. All the UCL lifetimes of the $^4S_{3/2}$ and $^4F_{9/2}$ states in $NaYF_4$:Yb,Er nanocrystals containing various Fe^{3+} ions from 5 mol% to 40 mol% are longer than that in the Fe^{3+}-free sample, and the maximum lifetime for both green and red UC emissions are found in the sample doped with 20 mol% Fe^{3+} ions. This trend of the lifetime variation is in good agreement with that of the integrated UCL intensity variation as shown in Figure 3. The slight improvement of decay-time constants with the increase of Fe^{3+} concentrations can be attributed to supplementary population due to the high excited energy state ET processes of other Yb^{3+}-Fe^{3+} dimer complex and Er^{3+} ions.[20] Whereas the suppression of lifetime when Fe^{3+} concentration reaches 20 mol% can be ascribed to the increased nonradiative transition probability induced by the extra defects stemming from heavy doping of Fe^{3+} as well as the exchange interaction between Fe^{3+} ions.

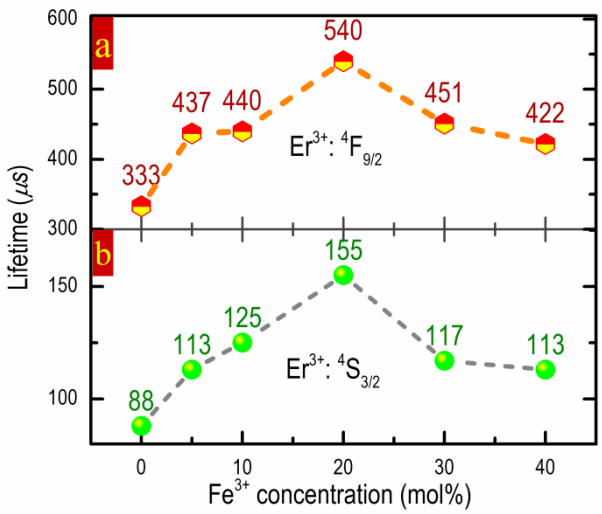

Fig. 7 Dependence of Er^{3+}: $^4F_{9/2}$ (a) and $^4S_{3/2}$ (b) UCL lifetimes on Fe^{3+} concentration in $NaYF_4$:18%Yb, 2%Er, xFe nanocrystals (x=0, 5, 10, 20, 30 and 40 mol%) under the excitation of a 10 ns pulsed laser at 980 nm from OPO, respectively.

Conclusions

Compared to a limited scale of increase of the green emission intensity a selective enhancement of UC red emission of $NaYF_4$:Yb,Er nanocrystals as well as the simultaneous manipulation of phase/size has been achieved via Fe^{3+} codoping. A potent mechanism involved energy transfer between the possible Yb^{3+}-Fe^{3+} dimer to Er^{3+} along with the distortion of crystal lattices has been proposed to understand the unique facts of the enhanced intensity of the red emission, red-to-green ratio and the overall UC when Fe^{3+} doping contents varies from 5 mol% to 20 mol%. The results provide an alternative approach to realize selective enhancement of desired UCL through transition metal codoping and taking advantage of the energy transfer sensitizing effect of Yb-transition metal complex, thus make this tri-doped UCNCs promising in multimodal bioimaging.

Acknowledgement

This work was supported by the National Natural Science Foundation of China (No. 11474035) and 2015 programming projects on scientific research of Jilin province department of education.

Notes and references

[a] *School of Basic Sciences & Advanced Institute of Materials Science, Changchun University of Technology, 2055 Yan'an Street, Changchun, Jilin 130012, P.R.China. Email: chenli@ccut.edu.cn*
[b] *State Key Laboratory of Luminescence and Applications, CIOMP, Chinese Academy of Sciences, Changchun, 130033, Jilin, China.*
[c] *Department of Physics, Georgia Southern University, Statesboro, Georgia 30460,USA.*

1. M. F. Joubert, S. Guy and B. Jacquier, *Physical Review B*, 1993, **48**, 10031-10037.
2. E. M. Dianov, *Light Sci Appl*, 2012, **1**, e12.
3. E. Downing, L. Hesselink, J. Ralston and R. Macfarlane, *Science*, 1996, **273**, 1185-1189.
4. B. Tian, B. Chen, Y. Tian, X. Li, J. Zhang, J. Sun, S. Fu, H. Zhong, X. Zhang, H. Yu and R. Hua, *Materials Express*, 2013, **3**, 241-246.
5. W. Zou, C. Visser, J. A.Maduro, M. S. Pshenichnikov and J. C. Hummelen, *Nature Photonics*, 2012, 560-564.
6. G.-B. Shan and G. P. Demopoulos, *Advanced Materials*, 2010, **22**, 4373-4377.
7. B. E. Cohen, *Nature*, 2010, **467**, 407-408.
8. P. Yuan, Y. H. Lee, M. K. Gnanasammandhan, Z. Guan, Y. Zhang and Q.-H. Xu, *Nanoscale*, 2012, **4**, 5132-5137.
9. P. Huang, W. Zheng, S. Zhou, D. Tu, Z. Chen, H. Zhu, R. Li, E. Ma, M. Huang and X. Chen, *Angewandte Chemie (International ed. in English)*, 2014, **53**, 1252-1257.
10. Q. Liu, W. Feng and F. Li, *Coordination Chemistry Reviews*, 2014, **273–274**, 100-110.
11. J. Wang, F. Wang, C. Wang, Z. Liu and X. Liu, *Angewandte Chemie International Edition*, 2011, **50**, 10369-10372.
12. X.-F. Yu, L.-D. Chen, M. Li, M.-Y. Xie, L. Zhou, Y. Li and Q.-Q. Wang, *Advanced Materials*, 2008, **20**, 4118-4123.
13. G. Tian, Z. J. Gu, L. J. Zhou, W. Y. Yin, X. X. Liu, L. Yan, S. Jin, W. L. Ren, G. M. Xing, S. J. Li and Y. L. Zhao, *Advanced Materials*, 2012, **24**, 1226-1231.
14. F. Auzel, *Chemical Reviews*, 2004, **104**, 139-174.
15. N. Niu, P. Yang, F. He, X. Zhang, S. Gai, C. Li and J. Lin, *Journal of Materials Chemistry*, 2012, **22**, 10889-10899.
16. J. H. Zeng, J. Su, Z. H. Li, R. X. Yan and Y. D. Li, *Advanced Materials*, 2005, **17**, 2119-2123.
17. A. Yin, Y. Zhang, L. Sun and C. Yan, *Nanoscale*, 2010, **2**, 953-959.
18. J.-C. Boyer, F. Vetrone, L. A. Cuccia and J. A. Capobianco, *Journal of the American Chemical Society*, 2006, **128**, 7444-7445.
19. J. F. Suyver, A. Aebischer, D. Biner, P. Gerner, J. Grimm, S. Heer, K. W. Krämer, C. Reinhard and H. U. Güdel, *Optical Materials*, 2005, **27**, 1111-1130.
20. Z. P. Li, B. Dong, Y. Y. He, B. S. Cao and Z. Q. Feng, *Journal of Luminescence*, 2012, **132**, 1646-1648.
21. D. Z. Ho Kim Dan, Rongfei Wang, Qing Jiao, Zhengwen Yang, Zhiguo Song, Xue Yua, Jianbei Qiu, *Optics & Laser Technology*, 2014, **64**, 264-268.
22. S. Ye, Y.-j. Li, D.-c. Yu, G.-p. Dong and Q.-Y. Zhang, *Journal of Materials Chemistry*, 2011, **21**, 3735-3739.
23. S. Zeng, Z. Yi, W. Lu, C. Qian, H. Wang, L. Rao, T. Zeng, H. Liu, H. Liu, B. Fei and J. Hao, *Advanced Functional Materials*, 2014, **24**, 4051-4059.
24. E. J. He, H. R. Zheng, W. Gao, Y. X. Tu, Y. Lu, H. Tian and G. Li, *J. Nanosci. Nanotechnol.*, 2014, **14**, 4139-4146.
25. P. Ramasamy, P. Chandra, S. W. Rhee and J. Kim, *Nanoscale*, 2013, **5**, 8711-8717.
26. M. G. Brik, N. M. Avram and C. N. Avram, *Optical Properties of 3d-Ions in Crystals: Spectroscopy and Crystal Field Analysis*, 2013, 29.
27. X. Li, F. Zhang and D. Zhao, *Chem.Soc.Rev*, 2015, **44**, 1346-1378.
28. F. Wang, Y. Han, C. S. Lim, Y. Lu, J. Wang, J. Xu, H. Chen, C. Zhang, M. Hong and X. Liu, *Nature*, 2010, **463**, 1061.
29. Y. Ding, X. Zhang, H. Gao, S. Xu, C. Wei and Y. Zhao, *Journal of Alloys and Compounds*, 2014, **599**, 60-64.
30. J. Zhou, Q. Liu, W. Feng, Y. Sun and F. Li, *Chemical Reviews*, 2015, **115**, 395-465.
31. J. F. Suyver, J. Grimm, M. K. van Veen, D. Biner, K. W. Krämer and H. U. Güdel, *Journal of Luminescence*, 2006, **117**, 1-12.
32. M. Pollnau, D. R. Gamelin, S. R. Lüthi, H. U. Güdel and M. P. Hehlen, *Physical Review B*, 2000, **61**, 3337-3346.
33. Y. Tanabe and S. Sugano, *Journal of The Physical Society of Japan*, 1954, **9**, 766-779.
34. J. Zhang, Z. Hao, J. Li, X. Zhang, Y. Luo and G. Pan, *Light Sci Appl*, 2015, **4**, e239.
35. J. Li, J. Zhang, Z. Hao, X. Zhang, J. Zhao and Y. Luo, *Chemphyschem*, 2013, **14**, 4114-4120.